

Phase segregation in binary $\text{SiO}_2/\text{TiO}_2$ and $\text{SiO}_2/\text{Fe}_2\text{O}_3$ nanoparticle aerosols formed in a premixed flame

Sheryl H. Ehrman^{a)} and Sheldon K. Friedlander

Air Quality and Aerosol Technology Laboratory, Department of Chemical Engineering,
5531 Boelter Hall, University of California, Los Angeles, California 90095

Michael R. Zachariah

Chemical and Science Technology Laboratory, Building 221, Room B312, National Institute of
Standards and Technology, Gaithersburg, Maryland 20899

(Received 23 January 1998; accepted 11 August 1999)

Binary $\text{SiO}_2/\text{TiO}_2$ and $\text{SiO}_2/\text{Fe}_2\text{O}_3$ nanoparticle (diameter < 100 nm) aerosols of varying mole ratios of Ti or Fe to Si were generated in a premixed Bunsen-type aerosol flame reactor. The distribution of species within the particles was investigated using transmission electron microscopy, electron energy loss spectrometry, x-ray diffraction, and Fourier transform infrared spectroscopy. Phase segregation was observed to varying degrees in qualitative agreement with segregation expected from binary phase diagrams for the bulk systems. Differences between the $\text{SiO}_2/\text{TiO}_2$ and $\text{SiO}_2/\text{Fe}_2\text{O}_3$ systems can be explained by considering the variation in the thermodynamically stable liquid-phase solubility and differences in the ability of iron and titanium ions to substitute for silicon ions in the network structure.

I. INTRODUCTION

Aerosol flame reactors have long been used for commercial scale production of single-component refractory oxide powders such as silica and titania.¹ The production of germanium-doped silica-based optical fibers by vapor-phase axial deposition is an example of an industrial scale multicomponent aerosol process.² We have a fairly good understanding of single-component aerosol formation from gas phase precursors in high-temperature processes. Growth occurs by collisions between primary particles followed by coalescence by either a viscous flow mechanism for liquid particles, or by solid-state diffusion if the particles are solid phase.^{3–6} Final primary particle size has been shown experimentally to depend on the time-temperature history of the process and on the material properties of the aerosols: viscosity for liquid particles or solid-state diffusivity.^{6–10}

Of particular interest in the formation of multicomponent aerosols is the arrangement of chemical species within the particles. For two-component systems many different arrangements are possible, some of which are shown in Fig. 1. These can range from differences in

chemical homogeneity, described by either the complete solubility of one oxide in another or the formation of a mixed solid oxide phase, to chemically distinct primary particles or agglomerates. The desired arrangement of species depends upon the application. For example, applications such as superparamagnetic powders for use in magnetic refrigeration technology require dispersion of small domains of the magnetic species in a nonmagnetic matrix.¹¹ Other applications such as low thermal expansion glass require complete solution of titania in silica.¹² Using high-temperature aerosol reactors, it is possible to produce large quantities of composite powders in a single step, an advantage over liquid phase synthesis routes. However, in order to produce materials meeting the requirements of specific applications, it is necessary to understand the factors determining the arrangement of species during the aerosol processing step.

Toward this goal, we report on the formation of $\text{SiO}_2/\text{TiO}_2$ and $\text{SiO}_2/\text{Fe}_2\text{O}_3$ nanoparticles ($d_p < 100 \text{ nm}$) in a premixed methane flame reactor at varying precursor mole ratios of Ti or Fe to Si. The distribution of species within the particles was investigated using transmission electron microscopy (TEM), electron energy loss spectrometry (EELS), x-ray diffraction (XRD), and Fourier transform infrared spectroscopy (FTIR). In earlier studies of the formation of $\text{SiO}_2/\text{TiO}_2$ composite particles in diffusion flames, segregation of the oxide species was observed within the primary particles and was linked to the formation of the condensable species at different locations in the flame.^{13,14} In previous studies of the for-

^{a)}Address all correspondence to this author.

Present address: Department of Chemical Engineering, University of Maryland, College Park, MD 20742-2111.
e-mail: sehrman@eng.umd.edu

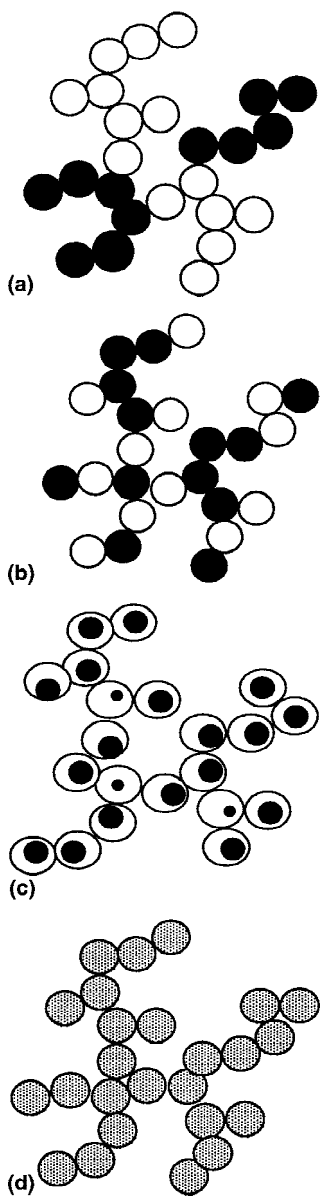


FIG. 1. Possible arrangements of chemical species in a binary aerosol: (a) distinct agglomerates, (b) distinct primary particles, (c) a coating of one species on another, (d) chemically homogeneous primary particles.

mation of these $\text{SiO}_2/\text{TiO}_2$ and $\text{SiO}_2/\text{Fe}_2\text{O}_3$ materials in premixed methane flames,^{15–18} segregated regions rich in the crystalline species, either titania or iron oxide, were also observed within the particles. As discussed by Ehrman *et al.*,¹⁸ precursor decomposition in a premixed flame environment is expected to be dominated by reactions involving radical species. Therefore, it will be very fast relative to particle formation processes, with little relative variation among precursor compounds. Hence, the appearance of segregated regions was believed not to result from differences in precursor chemistry; instead, it was related to the equilibrium phase distribution for each

system. For the temperatures and mole ratios used in the previous premixed flame studies, the oxides were not miscible, and the most thermodynamically favored phase distribution corresponded to segregated phases. However, in the liquid region of the phase diagrams of both systems, there are regions of miscibility. In the present study, we further investigate the link between the thermodynamically favored phase distribution according to the phase diagrams for each system as given in the literature^{19,20} and the observed phase segregation in the resulting aerosol.

II. EXPERIMENTAL PROCEDURES

A schematic of the experimental apparatus for generation of $\text{SiO}_2/\text{TiO}_2$ and $\text{SiO}_2/\text{Fe}_2\text{O}_3$ aerosols from gas phase precursors is shown in Fig. 2. Hexamethyl disiloxane (HMDS, $\text{C}_6\text{H}_{18}\text{OSi}_2$, 98+, Aldrich Inc.), titanium(IV) chloride (TiCl_4 , 99.9%, Cerac Inc.), and iron pentacarbonyl [$\text{Fe}(\text{CO})_5$, 98+, Aldrich Inc.] were used as the precursors for SiO_2 , TiO_2 , and Fe_2O_3 , respectively.²¹ These liquids have a significant vapor pressure at room temperature (greater than 12 torr) and were delivered to the flame by bubbling dried filtered nitrogen through the room-temperature liquids. To measure the precursor delivery rate to the flame, gravimetric determinations were made using a condensation trap of the postbubbler nitrogen stream as a function of nitrogen flow rate through the bubbler.²² To remove particles formed by bubble bursting, a 25-mm-diameter Gelman type A/E glass fiber filter was installed downstream of the bubblers. Because of the reactivity of the precursor compounds, particularly TiCl_4 , with water, all gases were passed through desiccant containers containing anhydrous calcium sulfate (Drierite). The flow rates of the precursors were varied to produce the precursor concentrations in the flame as given in Table I. In each experiment, the total concentration of Ti, Fe, and Si in the flame remained constant: 1.3×10^{-4} mol/l of flame gas at standard temperature and pressure.

The reactions to form the oxides were carried out by passing the postbubbler gases into a premixed methane/nitrogen/oxygen flame aerosol reactor (Fig. 2). The flow rates of the gases at standard temperature and pressure (STP) were 0.53 l/min (LPM) of methane, 3.7 LPM of nitrogen, and 1.4 LPM of oxygen, controlled using mass flow controllers. All experiments were conducted under oxygen-rich conditions, with the ratio of oxygen to methane flow rates remaining constant at 2.6 to 1, to minimize any unwanted carbon contamination in the particles resulting from incomplete combustion of methane or the precursor species.

The nozzle and water-cooled jacket, required to prevent the nozzle tip from melting, were constructed of

bronze. Flow straightening screens positioned inside the nozzle produced a stable cone-shaped flame, approximately 1.5 cm high, anchored at the edges of the nozzle. A plug of glass wool at the base of the reactor also aided in producing a stable flame and in mixing the precursors and flame gases. The Reynolds number for the flow conditions at the nozzle outlet was 700, falling in the transition region between laminar and turbulent jets.²³ The inner surface of the nozzle was machined smooth prior to use in these experiments, and during the course of the experiments, no turbulence was observed in the flame structure.

This flame configuration was chosen over a stabilized configuration, e.g., a flat flame stabilized on a porous ceramic or sintered metal plug to minimize heat loss, thus enabling high flame temperatures to be achieved (>2300 K, above the melting temperatures of the oxides). A disadvantage of this unstabilized configuration is that, because of the cone-shaped flame, the temperature profile in the postflame region is not radially uniform, and some variation in particle size is expected as a result of the nonuniform time-temperature history in the flame.

Because the temperatures in the flame were greater than the melting temperatures of the thermocouple materials, a rough approximation of the temperature profile

along the centerline of the flame was obtained for conditions corresponding to the experiment with an Si:Fe ratio of 5:1 using a two-color optical pyrometer (Capinotec Instruments Inc.), shown in Fig. 3.

The aerosol was sampled for TEM by rapidly injecting a formvar-coated copper TEM grid directly into the flame at a height of 5.5 cm above the nozzle of the reactor or 4 cm above the maximum flame height along the centerline. Particles deposited onto the grid by thermophoresis.²⁴ If one takes the spread of the flame into account, but assumes a plug flow velocity profile,²² the residence time of the particles in the postflame region prior to sampling is estimated to be approximately one hundredth of a second. To investigate the growth of the segregated regions, particles were sampled at a height of 0.3 cm above the top of the cone-shaped flame, corresponding to a residence time of less than 1 ms, and also 12 cm downstream (conceivably after particle formation was complete) using a nitrogen-aspirated sampling probe and impacting the particles onto a TEM grid using the critical orifice of Hering low-pressure impactor.²⁵ At 12 cm downstream, cooling and dilution of the particle stream rendered thermophoretic sampling ineffective.

The particles were imaged using a Phillips EM400 transmission electron microscope, equipped with a

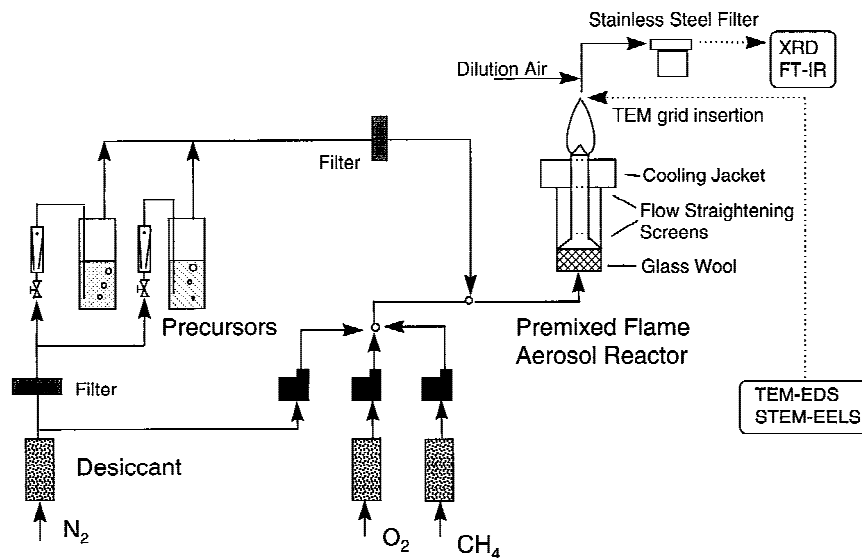


FIG. 2. Apparatus for generation of mixed aerosols in a premixed Bunsen-type burner.

TABLE I. Flow rates of precursor species.

Flow rate, 1 min^{-1} at STP	iron oxide only	silica only	titania only	8:1 Si:Ti	5:1 Si:Ti	1:1 Si:Ti	1:5 Si:Ti	10:1 Si:Fe	5:1 Si:Fe	1:1 Si:Fe	1:5 Si:Fe
Iron pentacarbonyl	0.022							0.0020	0.0037	0.0011	0.018
Hexamethyl disiloxane		0.011		0.0098	0.0092	0.0055	0.0018	0.010	0.0092	0.0055	0.0018
Titanium tetrachloride			0.022	0.0024	0.0037	0.011	0.018				

NORAN Explorer x-ray detector, allowing chemical analysis of the particles by energy dispersive x-ray spectrometry (EDS). To determine the composition of the segregated regions within the particles, EELS was conducted using a Fisons Instruments VG Microscopes HB501 scanning transmission electron microscope (STEM) equipped with a Gatan Model 666 energy electron loss spectrometer. The electron beam probe size ranged from 1 to 3 nm in diameter. Spatial resolution approximately equal to the probe diameter is achievable with EELS because electrons which are scattered out of the probe volume and therefore interacting with material outside of the probe volume are not detected.²⁶

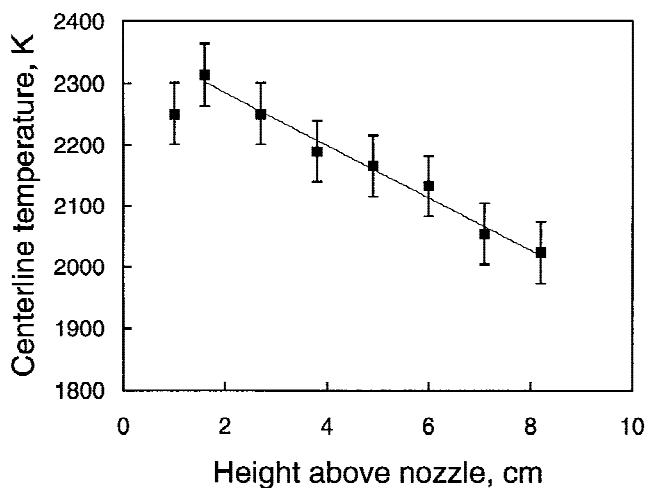


FIG. 3. Approximate temperature profile along the centerline of the flame, measured using two-color optical pyrometry. Error bars represent the estimated measurement uncertainty associated with this technique.

The particles were collected for x-ray diffraction and infrared spectroscopy analysis using a fritted 316 stainless steel 0.5 micron pore size filter, connected to house vacuum. The particles were sampled through a 0.64-cm outside diameter stainless steel tube from the center of the flame at a height of 5.5 cm above the nozzle. An equal volume of dilution air was introduced in a tee-joint 3 cm downstream to cool the particles, quenching formation and preventing further sintering of the particles after they deposited on the filter. The temperature of the filter unit was kept hot enough to prevent water from the flame from condensing in the filter unit, as evidenced by the absence of moisture on the filter deposit. The duration of each experiment was 30 min. A Phillips 1830H diffractometer was used for determination of the crystalline phases present in the particles. Powder samples were combined with KBr in a 1:200 mass ratio and pressed into pellets for analysis using a Mattson Research Series infrared (IR) spectrometer.

III. RESULTS AND DISCUSSION

A. Pure oxide species—TEM and XRD

Transmission electron micrographs of the single component oxide particles are shown in Fig. 4. X-ray diffraction patterns for the pure species are given in Figs. 5 and 6. Considerable variation in particle size was observed for each of the samples. This may be attributed in part to the radial variation of temperature in the cone-shaped flame. With the rapid insertion sampling technique employed here, particles are collected from the edge through to the flame centerline. Particles formed at the edge of the flame should cool more quickly and thus should be smaller than those formed along the centerline.

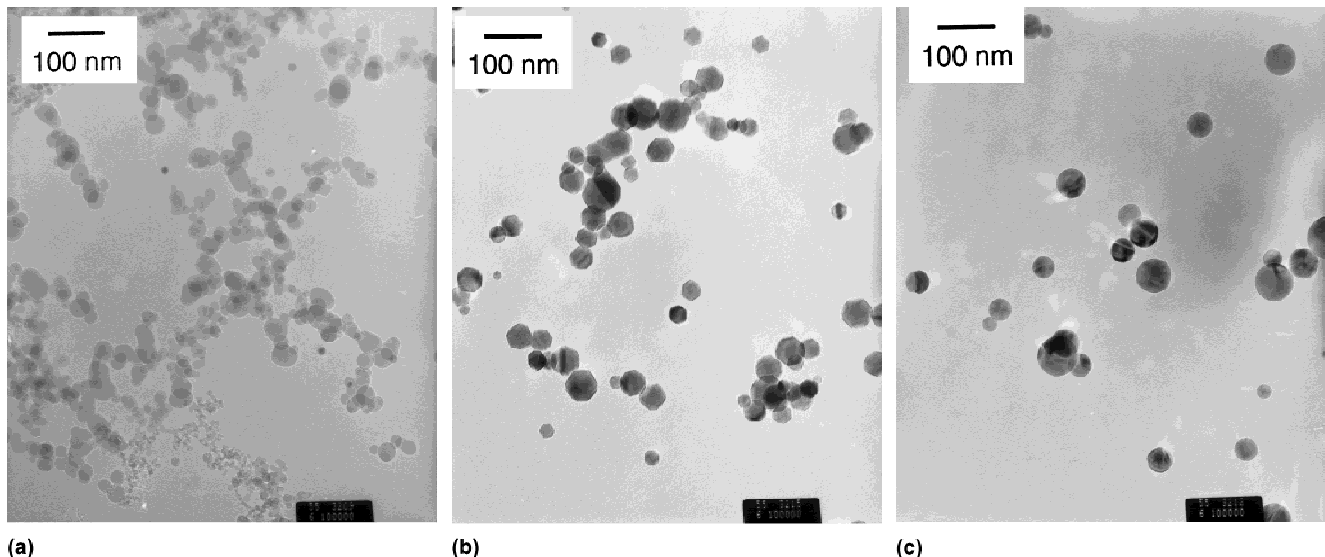


FIG. 4. TEM images of pure oxide aerosols: (a) silica from hexamethyl disiloxane, (b) iron oxide from iron pentacarbonyl, (c) titania from titanium tetrachloride.

The silica aerosol is agglomerated, with spheroidlike particles ranging in size from 8 to 60 nm. X-ray diffraction showed that the silica was amorphous. The titania particles are spherical, ranging in diameter from 20 to 70 nm, and mainly unagglomerated. Grain boundaries can be seen in some of the particles, possibly indicating incomplete sintering during particle growth. The x-ray diffraction pattern shows a trace of rutile phase present, but the particles are mainly anatase. The iron oxide par-

ticles are about the same size as the titania particles, ranging from 20 to 60 nm in diameter, but distinctly faceted rather than spherical. The x-ray diffraction patterns correspond to maghemite, $\gamma\text{-Fe}_2\text{O}_3$.

B. Mixed oxides—TEM and XRD

Transmission electron microscope images of the mixed $\text{SiO}_2/\text{TiO}_2$ oxides are shown in Fig. 7. In transmission electron microscopy, image contrast arises from differences in atomic number and crystallinity.²⁶ A crystalline area diffracts incident electrons, causing it to appear darker in the image than an amorphous region. The orientation of the crystalline region with respect to the electron beam may also affect contrast. In addition, if two particles are overlapping, the overlapped area will appear darker than the remainder of the particles.

The difference between the Ti-rich areas and the Si-rich areas is most apparent in the 1:5 Si to Ti sample [Fig. 7(d)]. Segregation is also easily observed in the 1:1 sample [Fig. 7(c)]. In the 5:1 Si to Ti sample [Fig. 7(b)], however, there are only a few very small Ti-enriched domains on the order of 5–10 nm in diameter, and in the 8:1 sample [Fig. 7(a)], there are no crystalline domains visible in the TEM image. EDS confirmed the mole ratios of Si to Ti in the particles were approximately equal to that in the feed. Confirmation of the enrichment of Ti in the dark regions was obtained by EELS analysis of the 1:1 samples.

In the 1:1 sample [Fig. 7(c)], there is curvature at the interface between the Si-rich and Ti-rich domains, which likely results from the difference in surface energies between SiO_2 and TiO_2 , 0.3 and 0.5 J m⁻², respectively.^{27,28} The observed morphology, if it is indeed the equilibrium arrangement, also gives information about the relative magnitude of the $\text{SiO}_2/\text{TiO}_2$ interfacial energy. In this arrangement, the interfacial area is just less than the free surface areas of SiO_2 and TiO_2 . This result suggests that the magnitude of the interfacial energy is comparable to the surface energies of SiO_2 and TiO_2 .

Transmission electron microscope images of the iron oxide/silica particles are shown in Fig. 8. Because of the greater difference in atomic number for Fe and Si (26 versus 14) as compared to Ti and Si (22 versus 14), the image contrast between the Fe-rich areas and the Si-rich areas is greater. The most notable difference between the two systems is that phase segregation is seen in every combination of Fe and Si, even in the 10:1 Si to Fe sample [Fig. 8(a)]. The size of the segregated regions ranges from 5 to 12 nm in the 5:1 Si:Fe sample [Fig. 8(b)] and 3 to 10 nm in the 10:1 Si:Fe sample [Fig. 8(a)]. Again, EDS confirmed the mole ratios of Si to Fe in the particles were approximately equal to that in the feed, and EELS confirmed enrichment of Fe in the dark regions by analysis of the 1:1 Si to Fe sample. In the

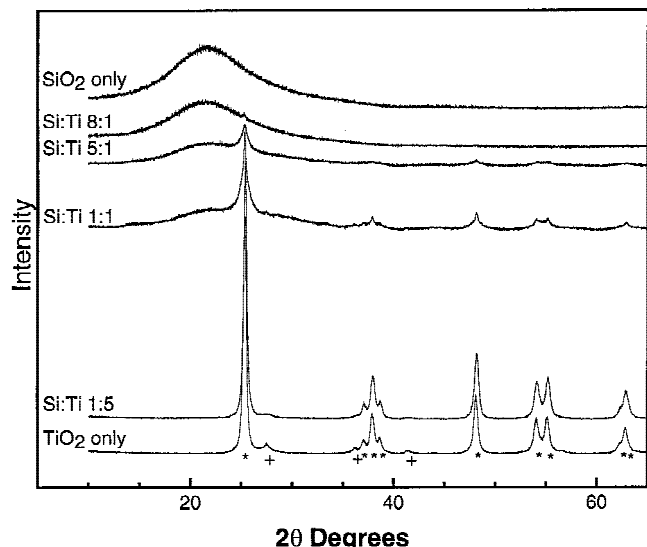


FIG. 5. XRD patterns of SiO_2 , TiO_2 , and mixed $\text{SiO}_2/\text{TiO}_2$ aerosol; * indicates peaks corresponding to anatase, while + indicates peaks corresponding to rutile.

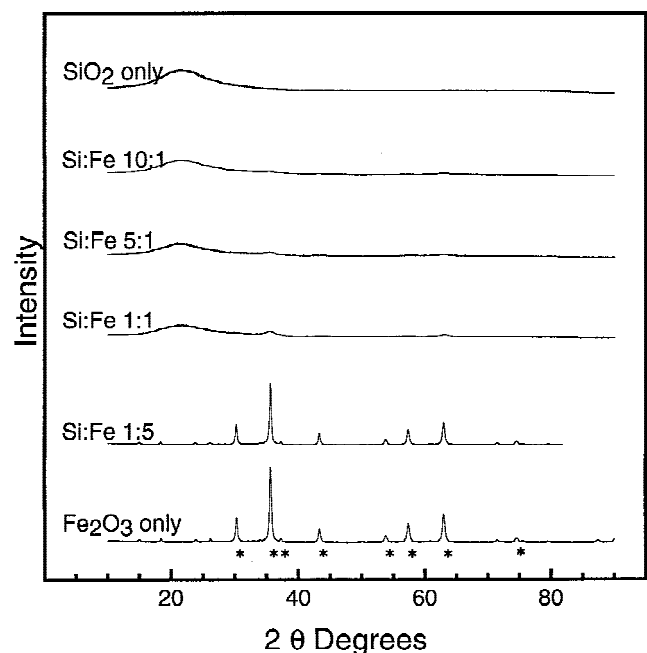


FIG. 6. XRD patterns of SiO_2 , Fe_2O_3 , and mixed $\text{SiO}_2/\text{Fe}_2\text{O}_3$ aerosol; * indicates peaks corresponding to $\gamma\text{-Fe}_2\text{O}_3$.

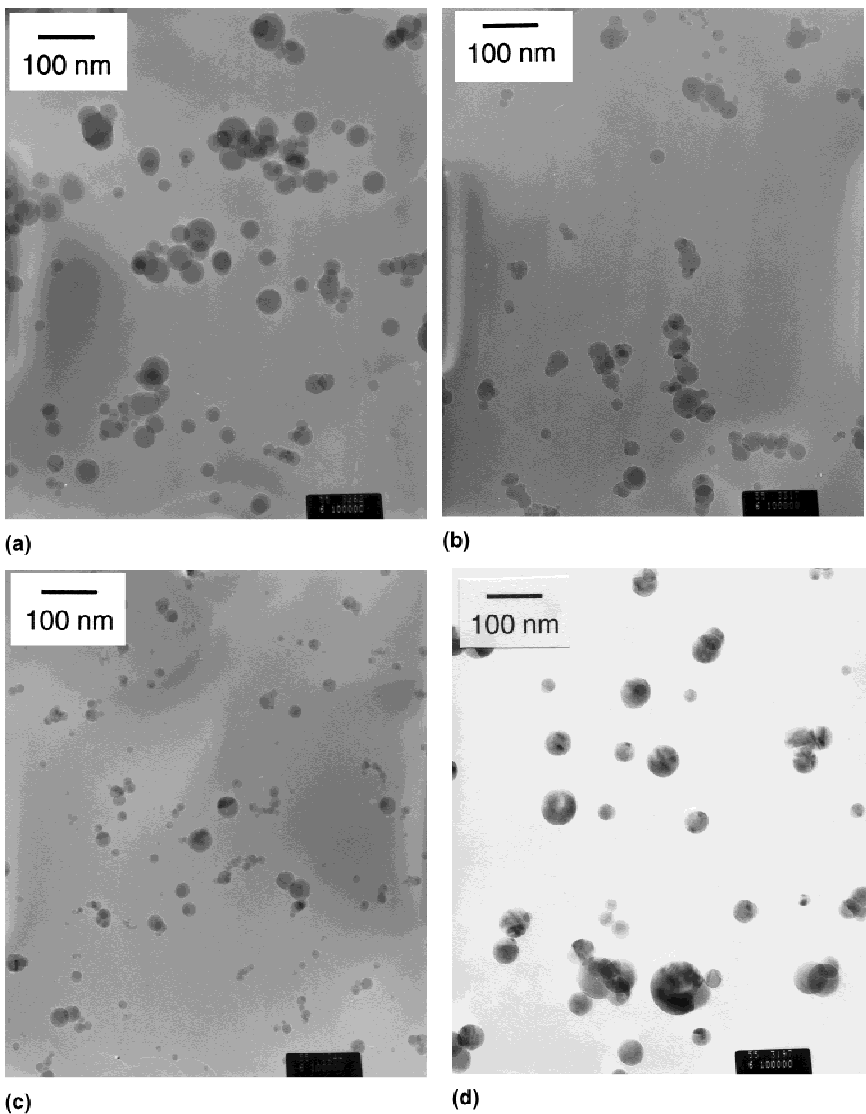


FIG. 7. TEM images of mixed $\text{SiO}_2/\text{TiO}_2$ samples: (a) Si:Ti ratio 8:1, (b) Si:Ti ratio 5:1, (c) Si:Ti ratio 1:1, (d) Si:Ti ratio 1:5.

1:1 samples, curvature is also seen at the interface between the Si-rich and the Fe-rich domains. The surface energy of Fe_2O_3 is 0.6 J m^{-2} ²⁹ greater than the surface energy of SiO_2 , with the arrangement of species also implying that the $\text{SiO}_2/\text{Fe}_2\text{O}_3$ interfacial energy is of the same magnitude as the SiO_2 and Fe_2O_3 surface energies.

The x-ray diffraction patterns shown in Figs. 5 and 6 corroborate the TEM results for phase segregation. Peaks corresponding to anatase TiO_2 are visible in the 5:1 Si to Ti sample (Fig. 5), and peaks corresponding to $\gamma\text{-Fe}_2\text{O}_3$ are observed in the 10:1 Si to Fe sample (Fig. 6). These peaks are broad, suggestive of small crystallite size.²⁶ As the concentration of Fe or Ti increases, the intensity of the peaks increases and the peak width narrows, suggesting the formation of larger segregated regions, also in agreement with TEM observations.

C. Mixed oxides—phase diagrams

We look to equilibrium thermodynamics to describe the segregation behavior of these particles in the initial stages of formation because, at and near the maximum temperature, the particles are small, and intraparticle diffusion is fast. As a result, the arrangement of species should be close to the distribution expected from equilibrium at the same temperatures. However, the cooling rate in this reactor is rapid, approximately 40 K/cm, corresponding to a maximum cooling rate of 33,000 K/s based upon the total gas flow rate through the nozzle at the maximum flame temperature of 2300 K. While equilibrium behavior may predict the arrangement of species, it cannot be expected to hold for the phase transitions as the particles cool. For example, we observe anatase and

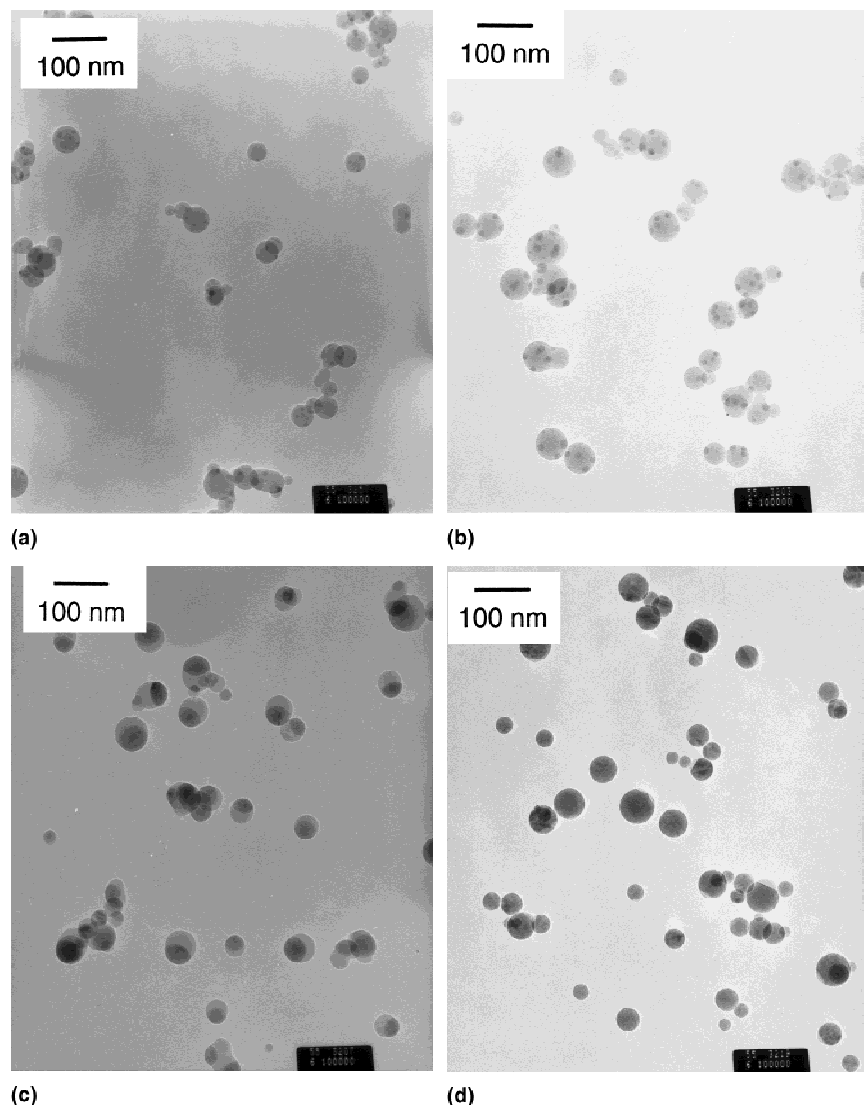


FIG. 8. TEM images of mixed $\text{SiO}_2/\text{Fe}_2\text{O}_3$ samples: (a) Si:Fe ratio 10:1, (b) Si:Fe ratio 5:1, (c) Si:Fe ratio 1:1, (d) Si:Fe ratio 1:5.

maghemite for the crystalline phases of titania and iron oxide, rather than rutile and hematite, which are the thermodynamically favored phases at room temperature.

The phase diagram for the silica/titania system is given in Fig. 9, adapted from DeVries *et al.*¹⁹ and presented as mol% Ti rather than wt% of TiO_2 in SiO_2 . The phase relationships in the iron oxide/silica system are not as straightforward. Iron readily exists in three different oxidation states, Fe^{3+} , Fe^{2+} , and Fe^0 . The composition of the condensed phases varies with the gas composition, as well as with condensed phase composition and temperature. For example, $\alpha\text{-Fe}_2\text{O}_3$ or hematite is the thermodynamically favored iron oxide phase at room temperature in air, but it transforms to Fe_3O_4 or magnetite upon heating. As a result, the iron oxide–silica system is truly ternary, $\text{FeO} \cdot \text{Fe}_2\text{O}_3\text{-SiO}_2$.³⁰ Because we are considering the formation of these mixed oxides in an

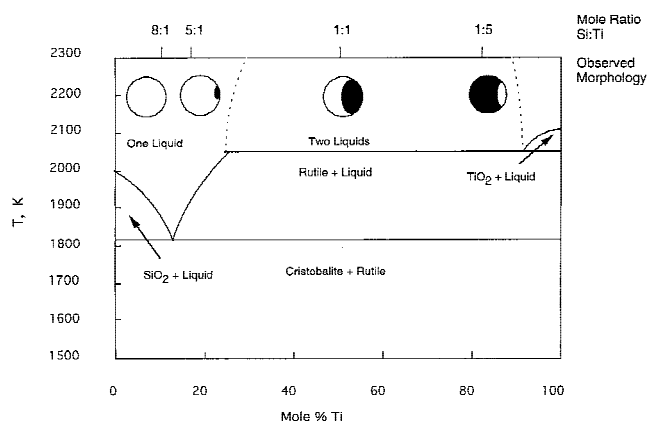


FIG. 9. Phase diagram of the $\text{SiO}_2/\text{TiO}_2$ system, adapted and modified from DeVries *et al.*¹⁹ Observed morphology for each mole ratio is shown.

oxygen-rich flame, we use the binary phase diagram for $\text{FeO} \cdot \text{Fe}_2\text{O}_3 - \text{SiO}_2$ in air adapted from Phillips and Muan²⁰ and given in Fig. 10.

If we compare both of the phase diagrams, several features are apparent. The most obvious feature common to both systems is the absence of a thermodynamically favorable mixed oxide phase. Also, for both systems, there is no solubility of one oxide in another in the solid phase. The ternary diagram for the $\text{FeO}-\text{Fe}_2\text{O}_3-\text{SiO}_2$ system shows the existence of a mixed iron silica phase, Fe_2SiO_4 (fayalite), but it is only favored in an oxygen-poor atmosphere.³⁰

Differences between the systems become apparent in examination of the liquid phase behavior. In the liquid phase, at a temperature of 2000 K, there is slight solubility of iron oxide in silica (10 mol%) and much greater solubility of titania in silica (20 mol%). As the temperature increases, the degree of solubility of the second oxide species in silica increases, but the solubility of titania in silica is always greater than that of iron oxide in silica. The phase diagrams as reported in the literature were determined experimentally and do not cover the entire temperature region of the flame so we have extrapolated the boundaries of the two-liquid region, also known as the miscibility gap.

For both systems, when the solubility limit is exceeded in the liquid phase, two immiscible liquids are the favored arrangement at equilibrium. Liquid–liquid immiscibility in glass systems has been studied extensively; see reviews by Stevens³¹ and Tomozawa.³² However, this bulk phenomenon has not been linked to the presence or absence of chemical segregation in flame-generated nanocomposite aerosols until recently.^{15,16,18} Warren and Pincus³³ first suggested that immiscibility in liquid silicates results from competition between the cations to surround themselves with a minimum energy oxygen an-

ion configuration. If the cation has limited capability to substitute for Si in the network, and also has a strong cation–oxygen bond strength, then the lowest energy configuration will consist of separate Si-rich and either Ti- or Fe-rich liquids.

Sketches of the observed segregation for each system are shown in Figs. 9 and 10. Experimentally, the most significant difference between the two systems is the absence of segregation in the 8:1 Si:Ti sample and the persistence of segregation in the $\text{SiO}_2/\text{Fe}_2\text{O}_3$ system down to the 10:1 Si:Fe sample. These results agree qualitatively with the distribution expected from the phase diagrams as titania is more soluble than iron oxide in silica in the liquid phase. Quantitative agreement would correspond to homogeneous samples for the mole ratios: Si:Ti 8:1, Si:Ti 5:1, Si:Fe 10:1, and Si:Fe 1:5. There are several possible explanations for why phase behavior other than the equilibrium behavior at the flame temperatures is observed. One reasonable explanation is the possibility of rearrangement of the species during quenching. The particles are formed at approximately 2300 K and cool to 2150 K at which point they are sampled for TEM/EELS or for XRD and FTIR. During sampling, the particles are rapidly quenched, and the extent of microstructural rearrangement occurring during the quenching step is not known.

Special phase behavior may result from the size of the nanoparticles. As discussed by Ehrman *et al.*,¹⁸ the pressure inside nanoparticles, resulting from the high surface to volume ratio, can be quite high, on the order of 2000 atm for a 10-nm particle of titania. It has been observed experimentally that, for some mixed silicates, the mobility of both Si^{4+} and O^{2-} ions in the melt *increases* as the external applied pressure increases, contrary to the behavior expected for crystalline systems with increasing pressure.^{34,35} Hence during quenching, phase segregation may be observed in nanoparticles but not bulk materials because of increased mobility associated with high internal pressure.

Experimentally, it appeared that the observed phase segregation in the $\text{SiO}_2/\text{TiO}_2$ system was predicted better by the phase diagram than was phase segregation in the $\text{SiO}_2/\text{Fe}_2\text{O}_3$ system. This suggests that differences in the mobility of Ti^{4+} and $\text{Fe}^{2+}/\text{Fe}^{3+}$ ions in liquid silica may determine how much microstructural rearrangement can take place. We refer to the iron ions as $\text{Fe}^{2+}/\text{Fe}^{3+}$ because only the as-cooled oxidation state of the iron (Fe^{3+}) is known, and both Fe^{2+} and Fe^{3+} may be present in the melt. Si^{4+} is considered a network forming species, existing in tetrahedral coordination with oxygen.²⁷ Ti^{4+} is considered an intermediate, capable of substituting for Si^{4+} in tetrahedral oxygen coordination to a limited extent in the network.^{27,36} Size and valence considerations favor the formation of $\text{Fe}^{2+}/\text{Fe}^{3+}$ in sixfold coordination with oxygen, and hence $\text{Fe}^{2+}/\text{Fe}^{3+}$ are considered net-

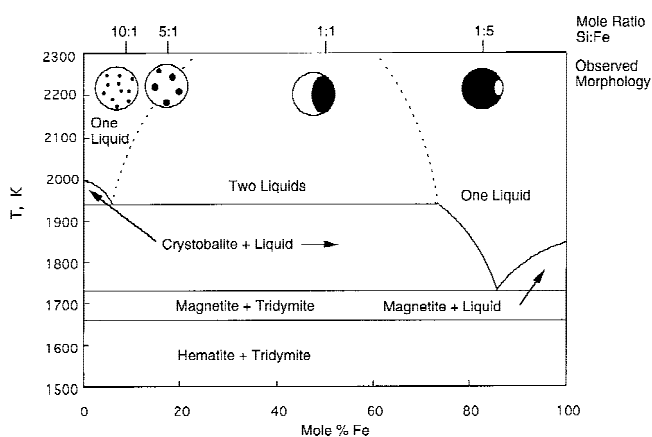


FIG. 10. Phase diagram of the $\text{SiO}_2/\text{FeO} \cdot \text{Fe}_2\text{O}_3$ system, adapted and modified from Phillips and Muan.²⁰ Observed morphology for each mole ratio is shown.

work modifiers, not able to contribute significantly to the network structure.³⁷ Therefore, during cooling, it is expected that the $\text{Fe}^{2+}/\text{Fe}^{3+}$ ions are more mobile than Ti^{4+} ions and should phase segregate to a greater extent, since some of the Ti^{4+} ions are expected to be chemically bound in the network structure.

D. Mixed oxides—FTIR and EELS

To probe the atomic arrangement of the Ti^{4+} and $\text{Fe}^{2+}/\text{Fe}^{3+}$ species, Fourier transform infrared spectra of the powders were obtained, and quantitative high-resolution EELS was conducted. IR spectra for $\text{SiO}_2/\text{TiO}_2$ and $\text{SiO}_2/\text{Fe}_2\text{O}_3$ are shown in Figs. 11 and 12. In the spectra of SiO_2 , bands corresponding to the symmetric (800 cm^{-1}) and asymmetric ($\sim 1100 \text{ cm}^{-1}$) stretch of the Si–O–Si bond are observed.³⁸ Beginning with the 8:1 Si:Ti sample (Fig. 11), an additional band at 960 cm^{-1} appears, characteristic of the Si–O–Ti stretch.³⁹ In the IR spectra of the $\text{SiO}_2/\text{Fe}_2\text{O}_3$ mixed oxides (Fig. 12), bands at 680 and 900 cm^{-1} characteristic of Si–O–Fe bonding^{40,41} do not appear in any of the samples. These results are expected on the basis of the previous discussion of the ability of the Ti^{4+} and $\text{Fe}^{2+}/\text{Fe}^{3+}$ to substitute into the network structure of silica.

Results of quantitative analysis of the 1:1 Si:Ti and 1:1 Si:Fe samples using EELS also corroborate the FTIR results. In this analysis, the number concentration (no. of atoms/electron beam cross-sectional area) of Fe or Ti and O atoms present was determined for both the crystalline regions and for the Si-rich regions within the particles.

In the 1:1 Si:Ti particles, the concentration of Ti atoms in the Si-rich region was fairly large, corresponding to an average Ti/O ratio of 0.14 ± 0.02 . In the 1:1 Si:Fe particles, with the exception of one analysis (Fe/O ratio of 0.07 ± 0.02), the concentration of iron atoms in the Si-rich region was below the threshold for detection associated with this technique (approximately Fe/O ratio of 0.05), indicating nearly complete segregation.

E. Proposed particle formation mechanism

In a premixed flame, all gases including the precursor species pass through the reaction zone of the flame. In this high-temperature environment ($T \sim 2300 \text{ K}$), reactions of the precursors are rapid and no significant differences in the chemical reaction behavior of the precursor species are expected. In the collision/coalescence model of particle growth, the driving force for coalescence of two particles is the reduction in surface free energy resulting from the formation of one sphere from two smaller spheres.⁴ Coalescence occurs by either a viscous flow mechanism if liquid or by solid-state diffusion. We propose that segregation within the particles is also occurring via liquid or solid-state diffusion as shown schematically in Fig. 13. The driving force for segregation is the reduction in the free energy of the system by the formation of the thermodynamically favored phase. The driving force for the growth of the individual domains is the reduction in the interfacial energy.

To investigate the formation of the segregated domains, an experiment was conducted with flow rates corresponding to a mole ratio of 5:1 Si to Fe in which we

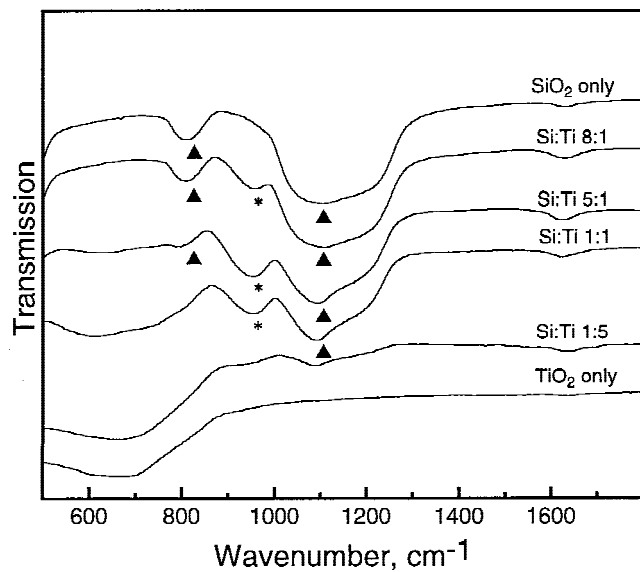


FIG. 11. FTIR spectra of SiO_2 , TiO_2 , and mixed $\text{SiO}_2/\text{TiO}_2$ samples. ▲ indicates absorption bands, which are characteristic of Si–O–Si bonding, while the band at $\sim 960 \text{ cm}^{-1}$, denoted by *, is characteristic of Si–O–Ti bonding.

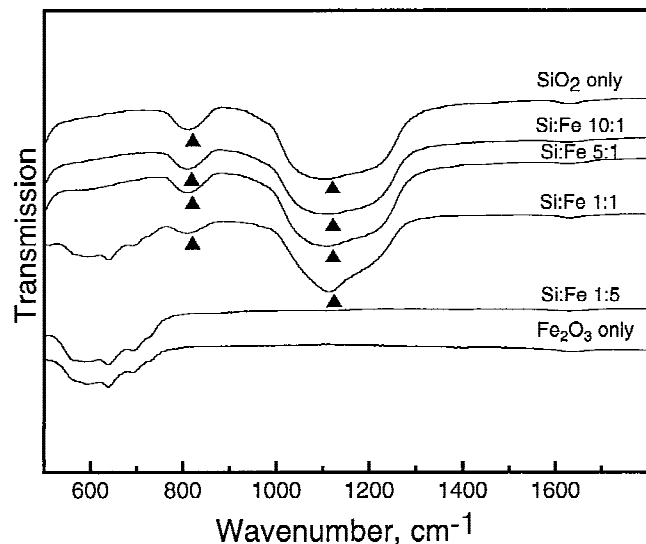


FIG. 12. FTIR spectra of SiO_2 , Fe_2O_3 , and mixed $\text{SiO}_2/\text{Fe}_2\text{O}_3$ samples. ▲ indicates absorption bands at 800 and $\sim 1100 \text{ cm}^{-1}$, which are characteristic of Si–O–Si bonding. No bands characteristic of Si–O–Fe bonding are visible in any of the spectra.

sampled at a distance of 0.3 mm from the tip of the flame cone and also 12 cm downstream. TEM images of the particles are shown in Fig. 14. In Fig. 14(a), many very small domains are visible, which appear to have formed by nucleation within the particles. In Fig. 14(b), the domains are larger with correspondingly fewer domains per particle, analogous to our proposed mechanism for formation. The dynamics of phase segregation have been simulated by Zachariah *et al.*¹⁶ using a molecular dynamics model with Lennard-Jones interaction potentials scaled to the melting points of silica, iron oxide, and iron silicate (used for the silica–iron oxide interaction). Their results show that, given enough time, the iron oxide clusters will eventually form a single cluster within the mixed particle. This implies that we are forming metastable structures in the flame and that, as shown in Fig. 14, the time–temperature history can be used as a variable to control the arrangement of species.

IV. CONCLUSIONS

Nanocomposite $\text{SiO}_2/\text{TiO}_2$ and $\text{SiO}_2/\text{Fe}_2\text{O}_3$ aerosols were formed in a premixed methane flame reactor. TEM images, EELS, XRD, and FTIR were used to determine the phases present and the arrangement of species in the particles. The observed segregation in the particles was compared to the segregation expected considering the equilibrium behavior of the systems at the flame temperatures. Qualitative agreement was seen between the distribution of species in the particles and that expected from the phase diagrams for the temperatures encountered in the flame, illustrating the usefulness of phase diagrams in predicting the distribution of species in aerosols formed in high-temperature processes. Differences between the $\text{SiO}_2/\text{TiO}_2$ and $\text{SiO}_2/\text{Fe}_2\text{O}_3$ systems can be explained by considering both thermodynamics and differences in the ability of $\text{Fe}^{2+}/\text{Fe}^{3+}$ and Ti^{4+} to substitute for Si^{4+} in the silica network. As shown by sampling at various residence times, time–temperature history is also an important variable affecting extent of segregation.

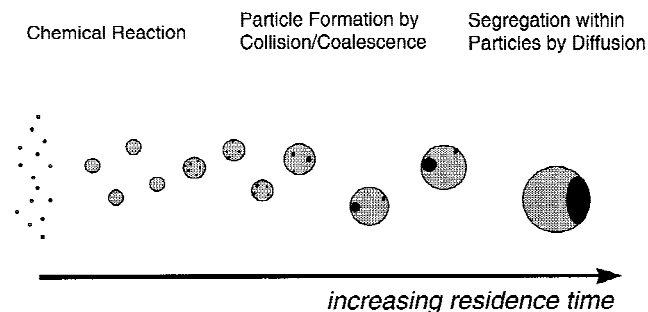
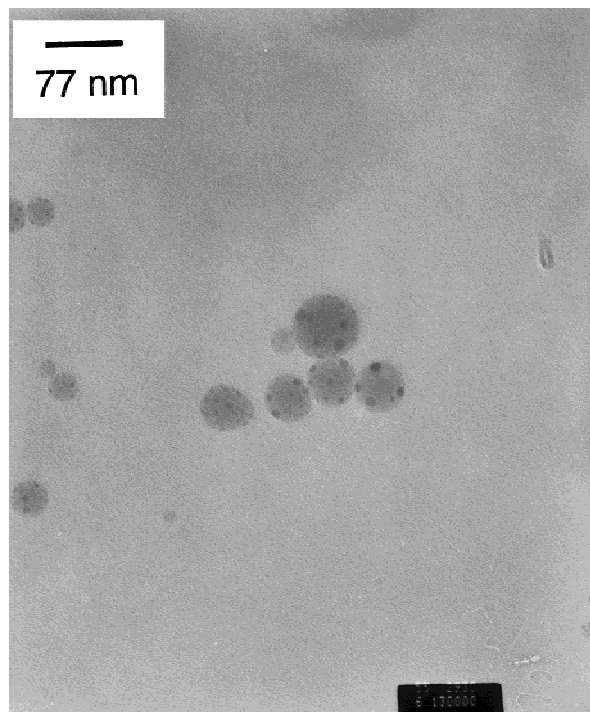
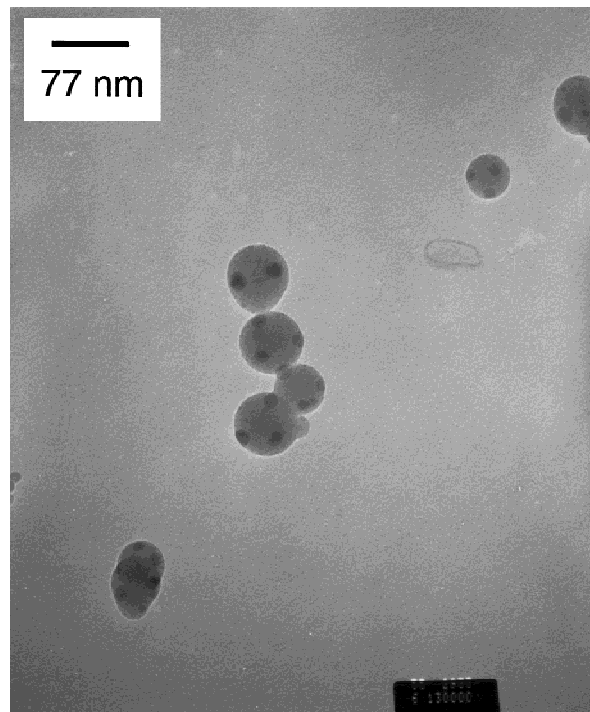


FIG. 13. Suggested particle formation mechanism. Particles grow by collision/coalescence. Segregation within the particles occurs by diffusion. The driving force is the reduction in free energy resulting from the formation of the thermodynamically favored phases.



(a)



(b)

FIG. 14. TEM images of mixed 5:1 Si:Fe particles, sampled (a) 3 mm above the tip of the flame and (b) 12 cm downstream. Tiny segregated domains are visible in the samples taken at 3 mm. The domains are larger in the 12-cm samples, with correspondingly fewer domains per particle.

ACKNOWLEDGMENTS

The authors wish to thank Dr. Dale Newbury of NIST for conducting the EELS analyses and Ms. Maria Aquino of NIST for conducting the x-ray diffraction analyses. This work was supported by the National Science Foundation under Grant No. CTS 92-18222.

REFERENCES

1. G.D. Ulrich, Chem. Eng. News, Aug 8 (1984).
2. T. Izawa and S. Sudo, *Optical Fibers: Materials and Fabrication* (KTK Scientific Publishers, Tokyo, 1987).
3. G.D. Ulrich and N.S. Subramanian, Combust. Sci. Technol. **17**, 119 (1977).
4. W. Koch and S.K. Friedlander, J. Colloid Interface Sci. **140**, 419 (1990).
5. S.K. Friedlander and M.K. Wu, Phys. Rev. B **49**, 3622 (1994).
6. J.J. Helble and A.P. Sarofim, J. Colloid Interface Sci. **128**, 348 (1989).
7. M.K. Wu, R.S. Windeler, C.K.R. Steiner, T. Börs, and S.K. Friedlander, Aerosol Sci. Technol. **19**, 527 (1993).
8. Y. Xiong, M.K. Akhtar, and S.E. Pratsinis, J. Aerosol Sci. **24**, 301–313 (1993).
9. R.S. Windeler, K.E.J. Lehtinen, and S.K. Friedlander, Aerosol Sci. Technol. **27**, 174 (1997).
10. R.S. Windeler, K.E.J. Lehtinen, and S.K. Friedlander, Aerosol Sci. Technol. **27**, 191 (1997).
11. R.D. Shull, R.D. McMichael, L.J. Swartzendruber, and L.H. Bennett, in *Magnetic Properties of Fine Particles: Proceedings of the International Workshop on Studies of Magnetic Properties of Fine Particles and their Relevance to Material Science*, edited by J.L. Dorman and D. Fiorani (North-Holland, Amsterdam, 1992).
12. P.C. Schultz, J. Am. Ceram. Soc. **59**, 214 (1976).
13. C-H. Hung and J.L. Katz, J. Mater. Res. **7**, 1861 (1992).
14. S. Vemury and S.E. Pratsinis, J. Am. Ceram. Soc. **78**, 2984 (1995).
15. M.R. Zachariah, M.I. Aquino, R.D. Shull, and E.B. Steel, Nanostruct. Mater. **5**, 383 (1995).
16. M.R. Zachariah, R.D. Shull, B.K. McMillin, and P. Biswas, in *Nanotechnology: Molecularly Designed Materials*, edited by G.M. Chow and K.E. Gonsalves (American Chemical Society, Washington, DC, 1995), pp. 42–63.
17. B.K. McMillan, P. Biswas, and M.R. Zachariah, J. Mater. Res. **11**, 1552 (1996).
18. S.H. Ehrman, S.K. Friedlander, and M.R. Zachariah, J. Aerosol Sci. **29**, 697 (1998).
19. R.C. DeVries, R. Roy, and E.F. Osborn, Trans. Brit. Ceram. Soc. **53**, 525 (1954).
20. B. Phillips and A. Muan, J. Am. Ceram. Soc. **42**, 413 (1959).
21. Mention of brand names does not imply or constitute endorsement by the National Institute of Standards and Technology.
22. S.H. Ehrman, Ph.D. Dissertation, University of California, Los Angeles, CA (1997).
23. B.K. Revill, in *Mixing in the Process Industries*, edited by N. Harnby, M.F. Edwards, and A.W. Nienow (Butterworth-Heinemann, Oxford, United Kingdom, 1992).
24. R.A. Dobbins and C.M. Megaridis, Langmuir **3**, 254 (1987).
25. S.V. Hering, R.C. Flagan, and S.K. Friedlander, Environ. Sci. Technol. **12**, 667 (1978).
26. J.P. Eberhart, *Structural and Chemical Analysis of Materials* (John Wiley & Sons, New York, 1991).
27. W.D. Kingery, H.K. Bowen, and D.R. Uhlmann, *Introduction to Ceramics* (John Wiley & Sons, New York, 1976).
28. R.H. Bruce, in *Science of Ceramics*, edited by G.H. Steward (Academic Press, 1965), Vol. 2.
29. G.V. Samsonov, *The Oxide Handbook*, 2nd ed. (IFI/Plenum, New York, 1982).
30. A. Muan, J. Met. **7**, 965 (1955).
31. H.J. Stevens, in *Introduction to Glass Science*, edited by L.D., H.J. Stevens, and W.C. LaCourse (Plenum Press, New York, 1972).
32. M. Tomozawa, in *Treatise on Materials Science and Technology, Vol. 17, Glass II*, edited by M. Tomozawa and R.H. Doremus (Academic Press, New York, 1979).
33. B.E. Warren and A.G. Pincus, J. Am. Ceram. Soc. **23**, 301 (1940).
34. N. Shimizu and I. Kushiro, Geochim. Cosmochim. Acta **48**, 1295 (1984).
35. B.T. Poe, P.F. McMillan, D.C. Rubie, S. Chakraborty, J. Yarger, and J. Diefenbacher, Science **276**, 1245 (1997).
36. R.B. Gregor, F.W. Lytle, D.R. Sandstrom, J. Wong, and P. Schultz, J. Non-Cryst. Solids **55**, 27 (1983).
37. A.A. Belyustin and A.M. Pisarevskii, in *The Structure of Glass*, edited by E.A. Porai-Koshits, (Proceedings of the Fourth All-Union Conference on the Glassy State, Leningrad, Consultants Bureau, New York, 1966).
38. A.J.M. de Man, B.W.H. van Beest, M. Leslie, and R.A. van Santen, J. Phys. Chem. **94**, 2524 (1990).
39. V.A. Zeitler and C.A. Brown, J. Phys. Chem. **61**, 1174 (1957).
40. R. Szostak, V. Nair, and T.L. Thomas, J. Chem. Soc., Faraday Trans. 1 **83**, 487 (1987).
41. D. Scarano, A. Zecchina, S. Bordiga, F. Geobaldo, G. Spoto, G. Petrini, G. Leofanti, M. Padovan, and G. Tozzola, J. Chem. Soc., Faraday Trans. 1 **89**, 4123 (1993).